

A Dynamic Charging System With Reduced Output Power Pulsation for Electric Vehicles

Fei Lu, *Student Member, IEEE*, Hua Zhang, *Student Member, IEEE*,
Heath Hofmann, *Senior Member, IEEE*, and Chunting Chris Mi, *Fellow, IEEE*

Abstract—This paper proposes a continuous dynamic wireless power transfer system for electric vehicles that reduces power pulsations during the charging process. Multiple rectangular unipolar coils are used at the primary side as the transmitters, and another unipolar coil works as a receiver at the secondary side. The transmitters are placed closely together to reduce the variation of magnetic fields along the moving track of the receiver. This structure induces self-coupling between the adjacent transmitters. An LCC-compensated circuit topology is utilized, and a compensation parameter design is provided which considers self-coupling between the primary coils. Finite-element analysis of the dynamic charging system is performed using Maxwell. The receiver size is optimized to reduce the variation of the coupling coefficient. A 1.4-kW dynamic charging prototype is constructed according to the designed coil structure and circuit parameters. There are six transmitters, each with dimensions 388 mm×400 mm, and one receiver with dimensions 485 mm×400 mm. Experimental results show that the output power pulsation is within $\pm 7.5\%$ in the dynamic charging process, and the maximum efficiency is 89.78%. If the edge effects of the transmitters are neglected, then the power pulsation is within $\pm 2.9\%$.

Index Terms—Continuous dynamic charging, dynamic charging, electric vehicle (EV), inductive power transfer (IPT).

I. INTRODUCTION

INDUCTIVE power transfer (IPT) is the most common approach to charging electric vehicles (EVs) wirelessly [1], [2]. It utilizes magnetic fields to transfer power to the

Manuscript received November 10, 2015; revised March 1, 2016; accepted April 9, 2016. Date of publication May 5, 2016; date of current version September 9, 2016. This work was supported in part by a U.S. Department of Energy Graduate Automotive Technology Education Grant, in part the U.S.-China Clean Energy Research Center—Clean Vehicle Consortium, in part by San Diego State University, in part by the University of Michigan, Ann Arbor, and in part by the China Scholarship Council.

F. Lu is with the Electrical Engineering and Computer Science Department, University of Michigan, Ann Arbor, MI 48109 USA, and also with the Department of Electrical and Computer Engineering, San Diego State University, San Diego, CA 92182 USA (e-mail: feilu@umich.edu).

H. Zhang is with the Department of Electrical and Computer Engineering, San Diego State University, San Diego, CA 92182 USA, and also with the School of Automation, Northwestern Polytechnical University, Xi'an 710072, China (e-mail: huazhang@umich.edu).

H. Hofmann is with the Electrical Engineering and Computer Science Department, University of Michigan, Ann Arbor, MI 48109 USA (e-mail: hofmann@umich.edu).

C. C. Mi is with the Department of Electrical and Computer Engineering, San Diego State University, San Diego, CA 92182 USA (e-mail: cmi@sdsu.edu).

Color versions of one or more of the figures in this paper are available online at <http://ieeexplore.ieee.org>.

Digital Object Identifier 10.1109/TIE.2016.2563380

vehicle through an air-gap distance of around 150 mm. The efficiency of the IPT system from the dc source to the dc load has reached higher than 96% at an output power of 7 kW [3], which makes the wireless charger comparable with wired charger technology.

Most of the present IPT systems focus on stationary charging applications. The vehicle is parked over the charger, and the receiver should be well-aligned with the transmitter. Otherwise, when there is a large misalignment between the receiver and transmitter, the output power and efficiency will drop significantly [4].

Dynamic charging is a promising technology that can help promote the adoption of EVs [5]. When the vehicle is moving on the roadway, it can be continuously powered. The driving range of the EV can be extended, and a smaller battery pack can be used in order to reduce the vehicle weight and improve transportation efficiency [6]–[8]. If 20% of the roads possess a 40-kW dynamic charging system, the driving range of an EV can be extended by at least 80% [9].

Dynamic charging systems can be classified according to the length of their transmitter coils: i.e., either long-track-loop transmitters [10]–[12] or short-individual transmitters [13]. The long-track-loop transmitter is usually between 10s to 100s of meters long, which is much longer than the vehicle length. Therefore, it can support multiple vehicles simultaneously [14], [15]. Its advantage is simplicity and a minimal number of circuit components. It is commercially available in Korea, where it is named the online electric vehicle (OLEV) [16], [17]. The total length of the transmitter is 90 m in a 3460 m route, and the maximum charging power is up to 100 kW [18]. To eliminate the radiated magnetic field, the transmitter can be twisted into an “X” shape [19], and an extra active field-canceling coil can be applied in addition to the transmitter [20]. In addition, the width of the transmitter and receivers can be designed to be asymmetric to improve the output power tolerance to lateral misalignment [21], [22]. In other designs, an additional quadrature coil is added to the receiver side to improve the misalignment ability even further [23], [24].

The limitation of the long-track-loop transmitter structure is its low efficiency. The maximum efficiency of the OLEV system is about 74% at 27 kW output [21]. This is because the inductance of the long transmitter is so large that the switching frequency is usually limited to 20 kHz. The quality factor $Q = \omega L/R$ of the long loop is therefore lower than the stationary system, which typically switches at 85 kHz [25]. Since the receiver is much smaller than the transmitter, the coupling coefficient is also small. Therefore, according to [26], the

efficiency of the long-track-loop dynamic charger is lower than the stationary chargers.

In the short-individual transmitter setting, the transmitter is the same size as the transmitter in the stationary charging system, which is usually within 1 m [27], [28]. Multiple short transmitters are arranged in an array to form a tracking lane for the vehicle. Since each transmitter coil has its own compensation network, it is more flexible to design the total length of the powered roadway. Also, the transmitters can be excited according to the receiver position. When the receiver leaves, the transmitters can be turned off, resulting in higher efficiency and lower magnetic field emissions [29], [30].

The limitation of the short-individual transmitter structure is its complexity, as it requires a large number of compensation components and power electronic converters. The total cost is higher than the long-track-loop system. Therefore, several coils can be connected in series or parallel to share the same power electronic converter in order to reduce system cost. Another drawback of the short structure is the power pulsations experienced by the receiver while moving. The primary transmitters are usually arranged far away from each other to eliminate the self-couplings among them. Therefore, the magnetic field is weak in the positions between the transmitters, and the received power drops when the receiver moves to a position between two transmitters. For example, in [29], the output power drops to nearly zero between two transmitters. One solution to reduce the power pulsation is to place the transmitters close to each other to increase the magnetic fields between them. The received power in the middle positions can therefore be increased. However, the power pulsations also exist in [27] and [28]. When the distance between the transmitters is about 30% of the transmitter length, the power pulsation is still 50% of the maximum power [28].

The limitation that prevents the transmitter coils coming closer is the self-couplings between them, which brings challenges to the compensation circuit design. In previous designs [27]–[29], the distance between the adjacent transmitters is large enough that the self-couplings can be neglected. If the separated distance keeps decreasing, the power pulsation is further reduced, and the self-couplings between the transmitters have to be considered in the compensation circuit design, which is an important contribution of this paper.

In this paper, six transmitter coils are arranged closely to reduce the power pulsation between two adjacent coils. The self-coupling between adjacent transmitters is considered when designing the circuit parameters. The size of the receiver coil is designed to minimize the power pulsations. Six transmitter coils are powered simultaneously by a single inverter to simplify the power electronics circuit structure. Each transmitter coil is compensated individually by its own compensation circuit, and is connected in parallel with other transmitter coils and their corresponding compensation circuits. In this structure, it is convenient to adjust the total length of the transmitters and it can also help to reduce the voltage stress on the compensation capacitors. With the designed coil size and circuit parameter values, the output power pulsation is within $\pm 2.9\%$ of the average power.

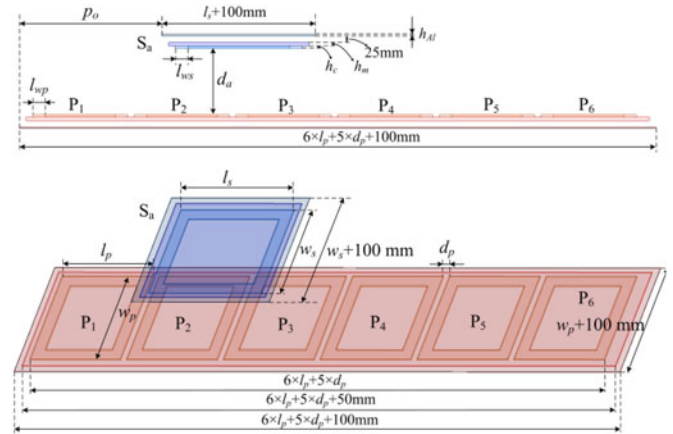


Fig. 1. Front view and 3-D view of the transmitters and receiver.

TABLE I
PARAMETERS DESCRIBING COIL STRUCTURE

Symbol	Explanation	Symbol	Explanation
l_p	Transmitter length	l_s	Receiver length
w_p	Transmitter width	w_s	Receiver width
l_{wp}	Transmitter winding width	l_{ws}	Receiver winding width
h_{Al}	Aluminum thickness	d_p	Transmitter space
h_m	Ferrite thickness	d_a	Air gap distance
h_c	Coil thickness	p_o	Receiver displacement

II. COIL DESIGN FOR CONTINUOUS DYNAMIC CHARGING

This paper adopts the short-individual transmitter approach to realizing the dynamic charging system. In this section, the structures and dimensions of the transmitters and receivers are provided. Finite-element analysis (FEA) simulations are performed using Maxwell to determine the self-inductances and the coupling coefficients of the coils.

A. Structure Design

The front and 3-D view of the coil structure are shown in Fig. 1, and the dimensions are also labeled in Fig. 1. There are six unipolar transmitters in our setup, labeled P_1 to P_6 . The receiver coil is also a unipolar structure, labeled as S_a . The definitions of the dimensions are described in Table I.

In our setup, Litz wire is used to build the coils, and ferrite plates are used with both the transmitter and receiver to increase the magnetic coupling. Furthermore, aluminum sheets are used to reduce magnetic field leakage. The thickness of the coils h_c is determined by the diameter of the Litz-wire. It contains 1900 strands AWG 38 wires and the total diameter is 6 mm. The thickness of the ferrite plate h_m is 5 mm, and the thickness of the aluminum h_{Al} is 2 mm. The distance between the ferrite plate and aluminum sheet is set to 25 mm to reduce the eddy current loss in aluminum sheet. The receiver displacement p_o is defined as the distance between the left edge of the receiver coil and the left edge of the transmitter coil.

Fig. 1 also shows that the length and width of the ferrite are 50 mm larger than the coil for better coupling. Meanwhile, the

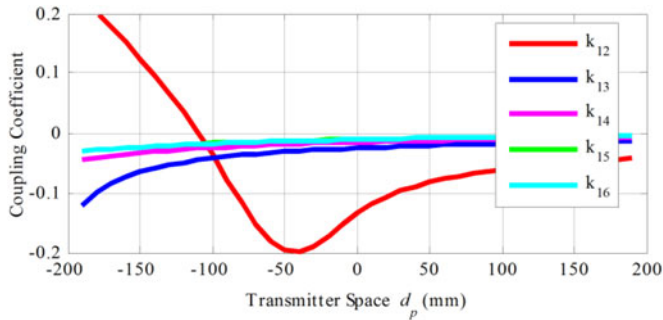


Fig. 2. Maxwell-simulated coupling coefficient between transmitters when space d_p varies.

length and width of the aluminum sheet are 50 mm larger than the ferrite to provide better shielding.

B. Transmitter Design

The main contribution of this paper is to study the self-coupling between transmitter coils, and design a compensation circuit for the coupled transmitters. Due to space limitations, the transmitter length l_p is set to 388 mm, the width w_p is set to 400 mm, and the coil width l_{wp} is set to 54 mm, which means that each coil has nine turns. Therefore, the transmitter coil spacing d_p is the only variable. The FEA simulated relationship between d_p and the coupling coefficient between the transmitters is shown in Fig. 2, where Maxwell was used.

All the transmitter coils are excited by currents flowing in the same direction. In Fig. 2, k_{12} indicates the coupling between adjacent transmitter coils, and the others indicate the coupling between nonadjacent coils. The sign of the coupling coefficient depends on the direction of the magnetic flux linkage coupled from one coil to the other [31]. In this system, since all six transmitter coils are identical and arranged in the same plane, the positive direction of the magnetic flux linkage can be defined when two transmitter coils are perfectly overlapped. Fig. 2 shows that the coupling coefficient k_{12} decreases from positive to negative with the parameter d_p , which defines the space between the transmitters. It shows that when the transmitter spacing d_p is positive, the adjacent coupling coefficient k_{12} is negative. As the spacing d_p decreases to negative values, which means the transmitter coils overlap, the coupling decreases to a minimum value. With further increasing overlap, the coupling increases to positive values. The couplings between nonadjacent transmitters are always negative as shown in Fig. 2.

Fig. 2 shows that when the adjacent transmitters have about 110 mm overlap, they are decoupled. However, $k_{13} = -0.045$, $k_{14} = -0.026$, $k_{15} = -0.018$, and $k_{16} = -0.017$, which means that the coupling with nonadjacent coils therefore cannot be neglected. The transmitter coils cannot be completely decoupled from one another. Furthermore, a 110 mm overlap means the transmitter loses 28% of its total effective length. In real applications, insulation between the overlapped coils is also an important concern. Therefore, the overlapped structure is not considered.

TABLE II
MAXWELL-SIMULATED COUPLING COEFFICIENT¹ AND MUTUAL INDUCTANCE²
BETWEEN TRANSMITTERS WHEN $d_p = 0$

M/k	1	2	3	4	5	6
1		-12.409	-2.4960	-1.4250	-1.0030	-0.9897
2	-0.14055		-11.2430	-1.9283	-1.1080	-1.0039
3	-0.02827	-0.12734		-11.106	-1.9265	-1.4241
4	-0.01614	-0.02184	-0.12579		-11.236	-2.4968
5	-0.01136	-0.01255	-0.02182	-0.12726		-12.407
6	-0.01121	-0.01137	-0.01613	-0.02828	-0.14053	

In this paper, the transmitter spacing d_p is set to 0, which means the transmitter coils are placed immediately next to each other. This structure effectively makes use of the coil length, and avoids low power areas between the transmitter coils. It can also help to reduce the variation of coupling coefficients between the transmitter coils and the receiver coil. The transmitters are negatively coupled, and the coupling coefficients and mutual inductances are shown in Table II. The lower left triangular data are the coupling coefficient, and the upper right triangular data are the mutual inductance in μH . For the mutual inductance, $M_{ij} = M_{ji}$ ($i \neq j$). The total mutual inductance of the i_{th} transmitter with the other transmitters is defined as M_i , which is shown as follows:

$$M_i = \sum_{j=1, j \neq i}^6 M_{ij}. \quad (1)$$

With the parameters in Table I, the mutual inductance of each transmitter is calculated as $M_1 = M_6 = -18.323 \mu\text{H}$, $M_2 = M_5 = -27.692 \mu\text{H}$, and $M_3 = M_4 = -28.195 \mu\text{H}$. Also, the self-inductance of the transmitter is $L_i = 88.29 \mu\text{H}$ ($i = 1, 2, \dots, 6$).

C. Receiver Design

As shown in Fig. 1, a unipolar coil is used as the receiver. For simplicity, the receiver width w_s and receiver coil width l_{ws} are designed to be the same as the transmitter coils, which means $w_s = 400$ mm and $l_{ws} = 54$ mm. The receiver length l_s is therefore the only variable considered.

When the receiver moves along the transmitter coils, power transfer occurs with each transmitter coil through magnetic coupling. The sum of their powers is the total received power, and the amount of power from each transmitter coil is determined by the coupling coefficient. One target of this design is to minimize the power variation in the dynamic charging process by optimizing the receiver size. If the receiver size is the same as the transmitter, $l_s = l_p = 388$ mm, the resulting coupling between the receiver and transmitter coils is shown in Fig. 3(a). The dashed lines represent the couplings with each transmitter, defined as k_{1a} , k_{2a} , k_{3a} , k_{4a} , k_{5a} , and k_{6a} , respectively. When the receiver moves close to one transmitter, they are positively coupled. When the receiver moves away, the coupling decreases to negative values. The total coupling k_a is shown as a solid red

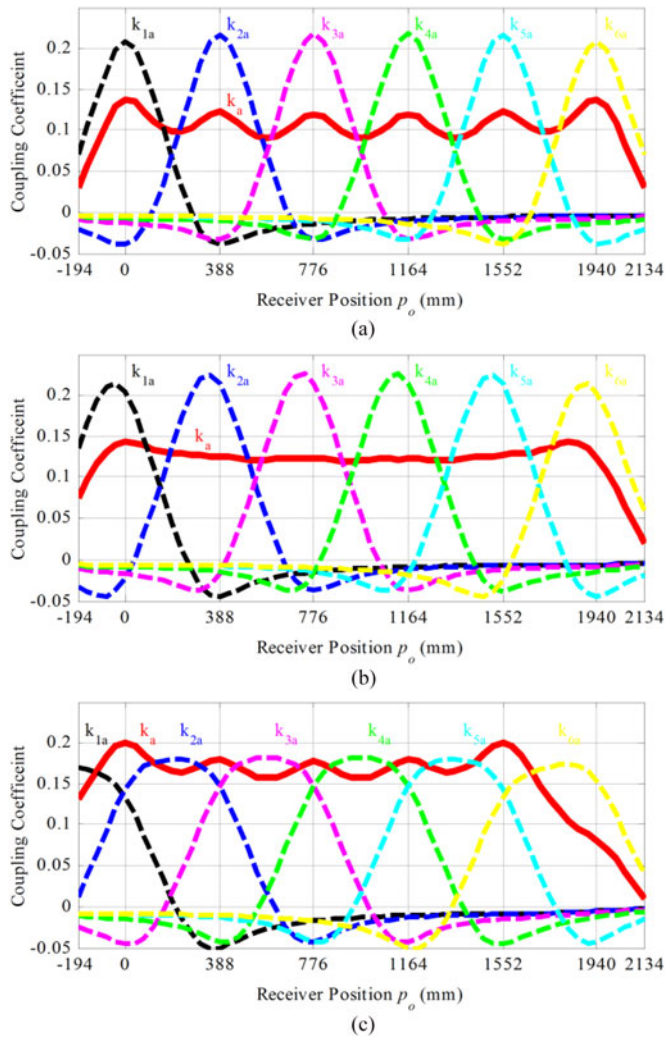


Fig. 3. Maxwell-simulated coupling coefficient between the receiver and transmitters at different receiver lengths l_s . k_{1a} , k_{2a} , k_{3a} , k_{4a} , k_{5a} , and k_{6a} are the coupling coefficients between receiver and each of the six transmitters. $k_a = k_{1a} + k_{2a} + k_{3a} + k_{4a} + k_{5a} + k_{6a}$ is the total coupling of receiver and transmitters. (a) Coupling coefficient when receiver length $l_s = 388$ mm. (b) Coupling coefficient when receiver length $l_s = 485$ mm. (c) Coupling coefficient when receiver length $l_s = 776$ mm.

line, and defined as follows:

$$k_a = k_{1a} + k_{2a} + k_{3a} + k_{4a} + k_{5a} + k_{6a}. \quad (2)$$

The total coupling is therefore the sum of six pulses, and there is variation in k_a due to the pulses. In the transmitter design, the spacing d_p between the transmitters has been set to zero to reduce the variation of coupling coefficient k_a . If the spacing d_p increases, the variation of k_a will also increase.

The receiver size was then increased to $l_s = 1.25 \times l_p = 485$ mm, and the resulting couplings are shown in Fig. 3(b). The shape of each individual coupling widens with the increasing receiver size. When they are added together, the variation of the total coupling k_a is reduced. Since the coupling coefficient relates to system power, this means that there will be

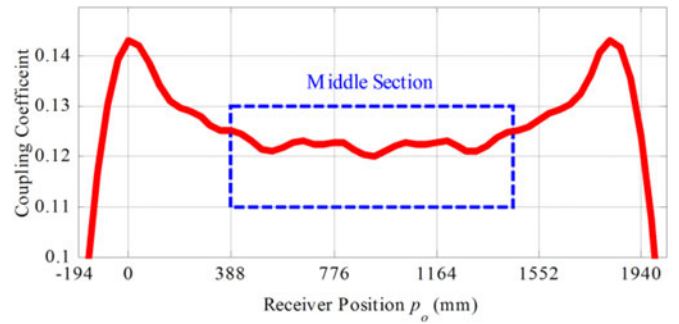


Fig. 4. Maxwell-simulated middle section of k_a when receiver length $l_s = 485$ mm.

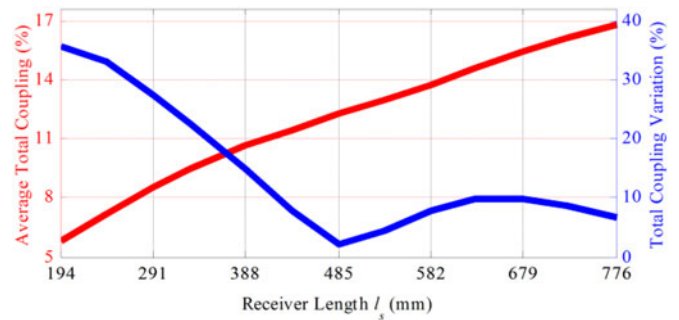


Fig. 5. Maxwell-simulated average value and variation of the total coupling coefficient k_a at different receiver length l_s .

little variation in the output power, and the vehicle can receive approximately constant power when it is driving on the roadway.

When the receiver size increases to $l_s = 2.0 \times l_p = 776$ mm, the couplings are shown in Fig. 3(c). The shape of each individual coupling becomes much wider. When they are added together, their variations cannot be canceled and the ripple in the total coupling k_a returns. Another important phenomenon shown in Fig. 3 is that there are two peaks in the total coupling k_a , when the receiver moves in and out of the transmitter coils. The details of Fig. 3(b) are shown in Fig. 4. Here, the two peaks at the ends are much more obvious. When the receiver moves to the ends, all the transmitters are on one side of the receiver, and there is lower negative coupling with the receiver. The output power is therefore larger compared to the other positions. The middle section is defined as $[l_p, 5 \times l_p - l_s]$, when the receiver moves to the second transmitter and away from the fifth transmitter. In the labeled middle section, the variation of the coupling coefficient is only $\pm 2.1\%$. In the middle section, considering the couplings in Figs. 3 and 4, the relation between the average coupling, coupling variation, and receiver length l_s is shown in Fig. 5.

When the receiver length l_s increases from 194 to 776 mm, the average total coupling coefficient k_a increases from 5.8% to 16.8%. However, the coupling variation is not monotonic with the receiver length. With increasing l_s , the variation first decreases to the minimum and then increases. The lowest variation occurs at 485 mm, so this value is chosen to realize the receiver. The average coupling k_a is 0.130, and the self-inductance of

TABLE III
DIMENSIONS AND INDUCTANCES OF TRANSMITTERS AND RECEIVER

Parameter	Design value	Parameter	Design value
l_p	388 mm	l_s	485 mm
w_p	400 mm	w_s	400 mm
l_{wp}	54 mm	l_{ws}	54 mm
h_{Al}	2 mm	d_p	0 mm
h_m	5 mm	d_a	150 mm
h_c	6 mm	Turn	9
L_i ($i = 1, 2, 3, 4, 5, 6$)	88.29 μH	L_a	105.46 μH
$M_{1,6}$	-18.323 μH	k_a	0.130
$M_{2,5}$	-27.692 μH	$M_{3,4}$	-28.195 μH

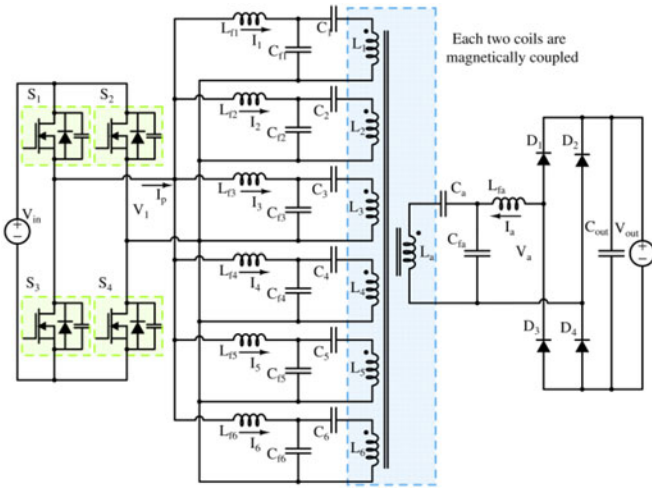


Fig. 6. Circuit topology of the double-sided *LCC*-compensated dynamic charging system.

the receiver $L_a = 105.46 \mu\text{H}$. When l_s increases larger than 679 mm, although the variation decreases, the receiver becomes more difficult to realize.

Using the design choices discussed above, the dimensions and inductance values of the transmitters and receiver are summarized in Table III.

III. *LCC* COMPENSATION CIRCUIT DESIGN FOR SELF-COUPLED TRANSMITTERS

The double-sided *LCC* compensation circuit topology is proposed in [25]. The advantage of this topology is that it performs as a current source to both the input and output, and it can maintain relatively high efficiency at both light and heavy load conditions. In the proposed self-coupled dynamic charging system, the *LCC* compensation topology is adopted, and the compensation circuit parameter design should consider all the couplings between transmitter coils. There are six coils at the transmitter side and one at the receiver side. When the power losses in all the components are neglected, the circuit is as shown in Fig. 6.

At the transmitter side, the input of the system is a dc source V_{in} , which is connected to a full-bridge inverter to apply a high-frequency ac voltage V_1 to the resonant circuit. Each transmitter

coil is compensated individually and then connected in parallel with other transmitters.

The parallel connection has two advantages. First, it provides the convenience to adjust the total length of the transmitter track. Especially in the long track application, it is flexible to add more transmitter coils connected in parallel with the existing transmitters without too much influence on the compensation circuit design. Second, it helps to reduce the voltage stress on the compensation capacitors. Since the transmitter coils are segmented, the voltage stress on each coil is reduced. Therefore, the voltage stress on the corresponding compensation capacitors for each transmitter is also reduced.

If all transmitter coils are connected in series, it will result in a large self-inductance at the primary side. In this structure, a single compensation circuit is enough and the circuit topology is therefore simplified. However, it is difficult to vary the length of the transmitter track, which requires disconnecting the existing circuit and redesigning the compensation circuit. Also, it is difficult to design the compensation capacitors due to the too large self-inductance of the long track transmitter. Therefore, the parallel connection is used in this paper to realize dynamic charging.

There are six resonant tanks at the transmitter side, corresponding to the six transmitter coils. Due to the self-coupling at the transmitter side, the resonance of each transmitter coil also relies on the coupling with other transmitters. The receiver coil is also compensated by an *LCC* network, followed by a full-bridge rectifier. The input voltage to the rectifier is a square wave, and the output load is the battery pack on the vehicle, which is represented by a voltage source V_{out} .

In the *LCC* network, L_f and C_f behave as a low-pass filter, so there is no high-order current injected into the coils. The fundamental harmonics approximation (FHA) method [25] is therefore used to analyze its working principle. The output voltage V_1 of the inverter and input voltage V_a of the rectifier are approximated as sinusoidal sources. Therefore, Fig. 6 is simplified as Fig. 7(a).

A. Working Principle of the Resonant Circuit

In Fig. 7(a), the magnetic coupling between the coils is represented by current-controlled voltage sources. Each transmitter is coupled with the other five transmitters and the receiver. The receiver is coupled with all six transmitters. The coupled voltage in a coil depends on the mutual inductances and the circulating current in the other coils.

Since the circuit in Fig. 7(a) is linear, the superposition theorem can be used to analyze the circuit; i.e., the two sources can be analyzed separately, and the results can be added together.

When the circuit is excited only by the input source, the resonances are shown in Fig. 7(b). L_{fa} and C_{fa} form a parallel resonance at the secondary side, and behave as an infinite impedance. The receiver coil is therefore treated as an open circuit; i.e., $I_{La} = 0$. The reflected voltages to the primary transmitters are all zero. The resonant frequency is designed to be the switching frequency f_{sw} , and the parameter relationship is

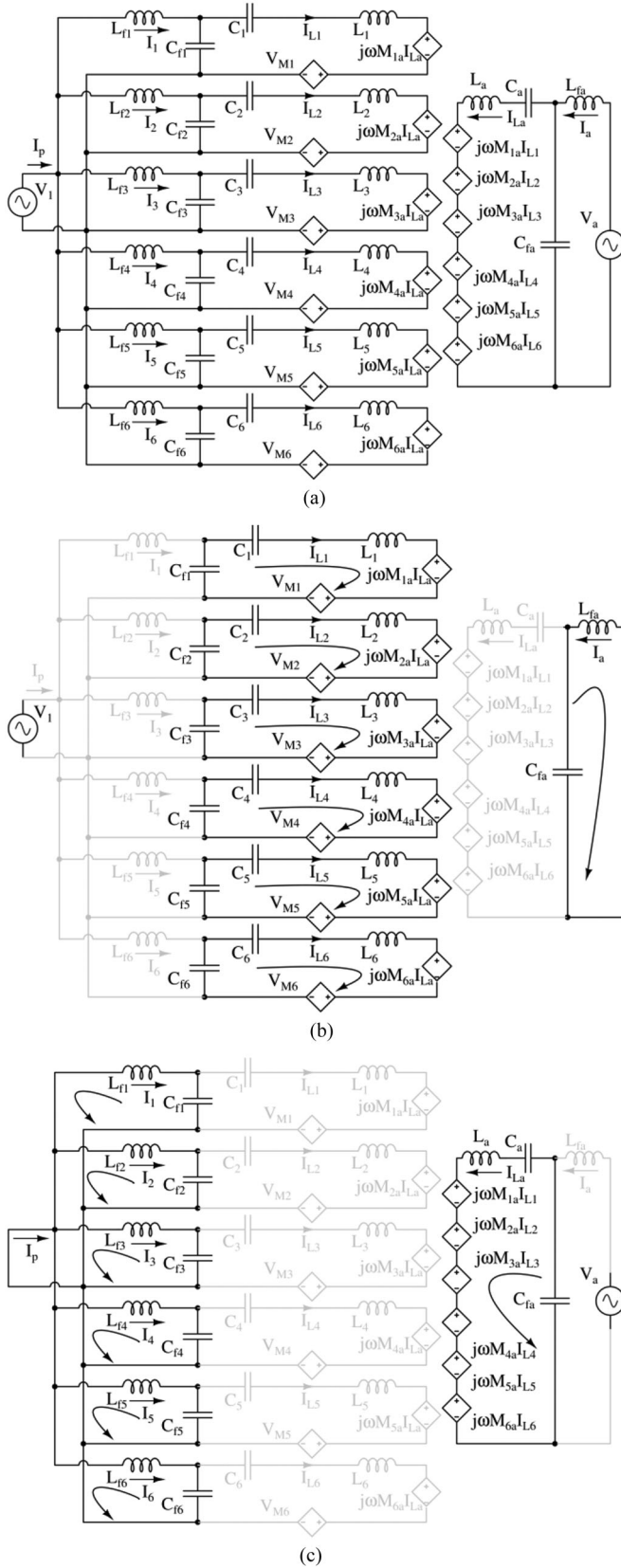


Fig. 7. FHA of the circuit. (a) Simplified resonant circuit. (b) Excited only by input source. (c) Excited only by output source.

expressed as

$$C_{fa} = 1/(\omega^2 L_{fi}) = 1/[(2\pi \cdot f_{sw})^2 L_{fi}]. \quad (3)$$

At the transmitter side, there are also six parallel resonances, considering all the self-coupling between transmitters. For each transmitter, the coupled voltage with the other transmitter coils can be expressed as

$$V_{M_i} = \sum_{j=1, j \neq i}^6 j\omega \cdot M_{ij} \cdot I_{L_j}, \quad i = 1, 2, 3, 4, 5, 6. \quad (4)$$

The impedances of the resonances are infinite to the input source \$V_1\$, and there is no current flowing through \$L_{f1,2,3,4,5,6}\$. Therefore, the parameters should satisfy the following equations, which is a design goal of the circuit parameters:

$$\begin{bmatrix} X_1 & M_{12} & M_{13} & M_{14} & M_{15} & M_{16} \\ M_{21} & X_2 & M_{23} & M_{24} & M_{25} & M_{26} \\ M_{31} & M_{32} & X_3 & M_{34} & M_{35} & M_{36} \\ M_{41} & M_{42} & M_{43} & X_4 & M_{45} & M_{46} \\ M_{51} & M_{52} & M_{53} & M_{54} & X_5 & M_{56} \\ M_{61} & M_{62} & M_{63} & M_{64} & M_{65} & X_6 \end{bmatrix} \cdot \begin{bmatrix} I_{L1} \\ I_{L2} \\ I_{L3} \\ I_{L4} \\ I_{L5} \\ I_{L6} \end{bmatrix} = 0 \quad (5)$$

where the equivalent self-reactance \$X_i\$ (\$i = 1, 2, 3, 4, 5, 6\$) of each loop shown in Fig. 7(b) is defined as

$$X_i = L_i - \frac{1}{\omega^2 C_i} - \frac{1}{\omega^2 C_{fi}}, \quad i = 1, 2, 3, 4, 5, 6. \quad (6)$$

At resonance, there is no current flowing through \$L_f\$, and so \$V_{C_{fi}} = V_1\$ (\$i = 1, 2, 3, 4, 5, 6\$). Then, the transmitter coil currents are calculated as

$$I_{L_i} = -\frac{V_1}{1/(j\omega C_{fi})} = -j\omega C_{fi} \cdot V_1, \quad i = 1, 2, 3, 4, 5, 6. \quad (7)$$

Considering (5) and (7), the relationship between \$X_i\$ and the capacitors \$C_{fi}\$ can be calculated as

$$\begin{bmatrix} X_1 \cdot C_{f1} \\ X_2 \cdot C_{f2} \\ X_3 \cdot C_{f3} \\ X_4 \cdot C_{f4} \\ X_5 \cdot C_{f5} \\ X_6 \cdot C_{f6} \end{bmatrix} = - \begin{bmatrix} 0 & M_{12} & M_{13} & M_{14} & M_{15} & M_{16} \\ M_{21} & 0 & M_{23} & M_{24} & M_{25} & M_{26} \\ M_{31} & M_{32} & 0 & M_{34} & M_{35} & M_{36} \\ M_{41} & M_{42} & M_{43} & 0 & M_{45} & M_{46} \\ M_{51} & M_{52} & M_{53} & M_{54} & 0 & M_{56} \\ M_{61} & M_{62} & M_{63} & M_{64} & M_{65} & 0 \end{bmatrix} \cdot \begin{bmatrix} C_{f1} \\ C_{f2} \\ C_{f3} \\ C_{f4} \\ C_{f5} \\ C_{f6} \end{bmatrix}. \quad (8)$$

In Fig. 7(b), although there is no current circulating in the receiver coil, there is voltage transferred to the receiver side, which is indicated in Fig. 7 and expressed as

$$V_{La} = \sum_{i=1}^6 j\omega \cdot M_{ia} \cdot I_{L_i} = \omega^2 \cdot V_1 \cdot \sum_{i=1}^6 M_{ia} \cdot C_{fi}. \quad (9)$$

Then, the output current in the inductor L_{fa} is calculated as

$$I_{Lfa} = -I_a = \frac{V_{La}}{j\omega \cdot L_{fa}} = \frac{-j\omega \cdot V_1}{L_{fa}} \sum_{i=1}^6 M_{ia} \cdot C_{fi}. \quad (10)$$

When the circuit is excited only by the output source, the result is shown in Fig. 7(c). Similarly to Fig. 7(b), there are also multiple parallel resonances highlighted in the circuit. At the primary side, they can be expressed as follows, which is another design goal of circuit parameters:

$$C_{fi} = 1/(\omega^2 L_{fi}) = 1/[(2\pi \cdot f_{sw})^2 C_{fi}], \quad i = 1, 2, 3, 4, 5, 6. \quad (11)$$

The parallel resonance of L_{fi} and C_{fi} behaves as an infinite impedance for the transmitter coils, so there is no current flowing through them.

On the secondary side, the capacitor C_a can be designed to maintain a parallel resonance in the receiver. The relationship between the parameters is shown as

$$C_a = \frac{1}{\omega^2 [L_a - 1/(\omega^2 C_{fa})]} = \frac{1}{\omega^2 (L_a - L_{fa})}. \quad (12)$$

In this case, there is no current flowing through L_{fa} , so the voltage on C_{fa} is also the output voltage V_a , and the circulating current in the receiver is given by

$$I_{La} = -\frac{V_a}{1/(j\omega C_{fa})} = -j\omega C_{fa} \cdot V_a. \quad (13)$$

The reflected voltage to each transmitter coil is expressed as

$$V_{Li} = j\omega \cdot M_{ia} \cdot I_{La} = \omega^2 \cdot M_{ia} \cdot C_{fa} \cdot V_a, \quad i = 1, 2, 3, 4, 5, 6. \quad (14)$$

The input current in the inductor L_{fi} is therefore calculated as

$$I_{Lfi} = -I_i = \frac{V_{Li}}{j\omega \cdot L_{fi}} = \frac{-j\omega \cdot M_{ia} \cdot C_{fa} \cdot V_a}{L_{fi}}. \quad (15)$$

The total input current I_p is the sum of $I_i (i = 1, 2, \dots, 6)$, and is expressed as follows:

$$I_p = \sum_{i=1}^6 I_i = j\omega \cdot C_{fa} \cdot V_a \cdot \sum_{i=1}^6 \frac{M_{ia}}{L_{fi}}. \quad (16)$$

From the previous analysis, it shows that the input current only depends on the output voltage, and the output current only depends on the input voltage. The circuit therefore performs as a current source for both the input and output.

B. Calculate System Power

The input and output currents are expressed in (10) and (16). A full-bridge diode rectifier is used at the receiver side. The phase of the output voltage V_a is determined by the inductor current I_{Lfa} . When the current I_{Lfa} is flowing, the output voltage V_a is clamped to V_{out} or $(-V_{out})$, depending on the direction of I_{Lfa} . The output voltage V_a and current I_{Lfa} are therefore in phase. Equation (10) shows that V_1 leads I_{Lfa} by 90° , and (15) shows that I_i leads V_a by 90° . Therefore, V_1 and I_i are also in phase. It means that unity power factor is realized for each transmitter coil.

Since the output voltage V_a is in phase with output current I_{Lfa} , the output power can be calculated from (10) as

$$P_{out} = |V_a| \cdot |I_{Lfa}| = \frac{\omega \cdot |V_1| \cdot |V_a|}{L_{fa}} \cdot \sum_{i=1}^6 M_{ia} \cdot C_{fi}. \quad (17)$$

Also, the input voltage V_1 and the input current I_i are in phase, and the input power can be calculated from (16) as

$$P_{in} = |V_1| \cdot |I_p| = \omega \cdot C_{fa} \cdot |V_a| \cdot |V_1| \cdot \sum_{i=1}^6 \frac{M_{ia}}{L_{fi}}. \quad (18)$$

According to the resonances indicated in (3) and (11), the input and output powers are equal to each other, which agrees with the previous assumption to neglect the component losses.

In Section II, the six transmitter coils are designed to be identical, and they are placed adjacent to each other. Therefore, their self-inductances and mutual inductances satisfy the following expression:

$$\begin{aligned} L_1 &= L_2 = L_3 = L_4 = L_5 = L_6 \\ M_{ij} &= M_{ji} (i, j = 1, 2, 3, 4, 5, 6, i \neq j) \\ M_{12} &= M_{23} = M_{34} = M_{45} = M_{56} \\ M_{13} &= M_{24} = M_{35} = M_{46} \\ M_{14} &= M_{25} = M_{36} \\ M_{15} &= M_{26}. \end{aligned} \quad (19)$$

The compensation parameters are chosen to be identical, i.e.,

$$\begin{aligned} L_{f1} &= L_{f2} = L_{f3} = L_{f4} = L_{f5} = L_{f6} = L_f \\ C_{f1} &= C_{f2} = C_{f3} = C_{f4} = C_{f5} = C_{f6} = C_f. \end{aligned} \quad (20)$$

Therefore, the system power in (17) and (18) is given by

$$P_{in} = P_{out} = \frac{M_{1a} + M_{2a} + M_{3a} + M_{4a} + M_{5a} + M_{6a}}{\omega \cdot L_f \cdot L_{fa}} \cdot |V_1| \cdot |V_a|. \quad (21)$$

Considering (2) and (19), it can be rewritten as

$$\begin{aligned} P_{in} = P_{out} &= \sum_{i=1}^6 k_{ia} \cdot \frac{\sqrt{L_1 \cdot L_a} \cdot |V_1| \cdot |V_a|}{\omega \cdot L_f \cdot L_{fa}} \\ &= \frac{k_a \cdot \sqrt{L_1 \cdot L_a} \cdot |V_1| \cdot |V_a|}{\omega \cdot L_f \cdot L_{fa}}. \end{aligned} \quad (22)$$

This shows that system power is proportional to the coupling coefficient, mutual inductance, and input and output voltages.

IV. 1.4-kW DYNAMIC CHARGING SYSTEM DESIGN

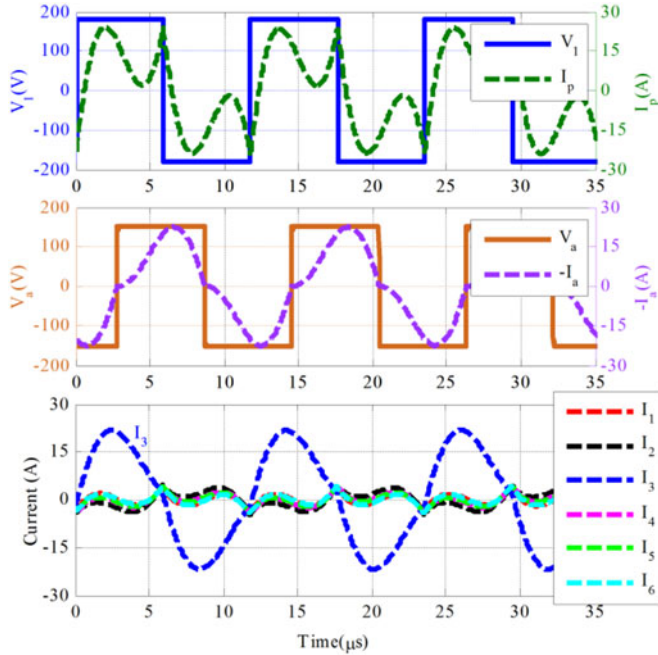
In this section, a 1.4-kW input power dynamic charging system is designed. The scaled-down power level is based on the capability and space limitation of our laboratory.

A. Circuit Parameter Design

The inductances of the coils have been provided in Table III, and the inductors L_{fi} and L_{fa} are determined according to the power in (21). To reduce the circulating current in the transmitters, L_{fi} is designed to be two times larger than L_{fa} . The values of capacitors C_{fi} and C_{fa} are provided in (3) and (11).

TABLE IV
 SYSTEM SPECIFICATIONS AND CIRCUIT PARAMETER VALUES

Parameter	Design value	Parameter	Design value
V_{in}	180 V	V_{out}	150 V
L_{fi} ($i = 1, 2, 3, 4, 5, 6$)	26.31 μ H	L_{fa}	13.15 μ H
C_{fi} ($i = 1, 2, 3, 4, 5, 6$)	133.28 nF	C_{fa}	266.55 nF
L_i ($i = 1, 2, 3, 4, 5, 6$)	88.29 μ H	L_a	105.5 μ H
C_1, C_6	80.30 nF	C_a	37.98 nF
C_2, C_5	102.24 nF	C_3, C_4	103.8 nF
f_{sw}	85 kHz	k_a	13.0%


Fig. 8. LTspice-simulated voltage and current waveforms.

Considering (3), (6), and (8), the capacitor C_i is given by

$$C_i = \frac{1}{\omega^2(L_i - L_{fi} + \sum_{j=1, j \neq i}^6 M_{ij})} = \frac{1}{\omega^2(L_i - L_{fi} + M_i)},$$

$$i = 1, 2, 3, 4, 5, 6. \quad (23)$$

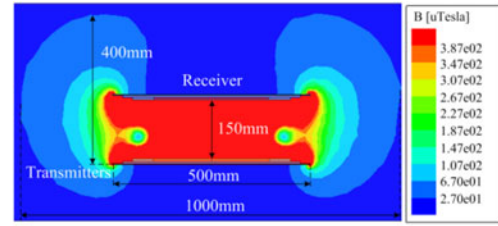
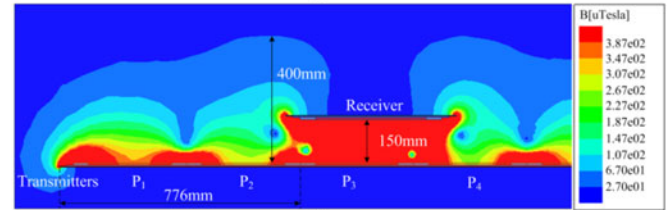
It needs to be emphasized that the high-order harmonic current [25] helps to achieve soft switching. Therefore, all the parameter values for a 1.4-kW dynamic charging system are shown in **Table IV**

B. System Simulation

With the parameters in **Table IV**, the circuit performance is simulated in LTspice. When the receiver position p_o is set to 776 mm, **Fig. 3(b)** shows the Maxwell simulated couplings between receiver and transmitters as $k_{1a} = -0.0138$, $k_{2a} = -0.0338$, $k_{3a} = 0.2180$, $k_{4a} = -0.0156$, $k_{5a} = -0.0144$, and $k_{6a} = -0.010$. The LTspice-simulated waveforms are shown in **Fig. 8**. This shows that the input current I_p is in phase with the

TABLE V
 SIMULATED PEAK VOLTAGE AND CURRENT STRESSES OF COMPONENTS

Parameter	Voltage	Current
MOSFETs	180 V	22 A
Diodes	150 V	22 A
C_{fi} ($i = 1, 2, 3, 4, 5, 6$)	400 V	30 A
C_i ($i = 1, 2, 3, 4, 5, 6$)	370 V	15 A
C_{fa}	300 V	40 A
C_a	1.3 kV	26 A


(a)

(b)
Fig. 9. Maxwell-simulated magnetic field emission. (a) Left view of the magnetic field. (b) Front view of the magnetic field.

input voltage V_1 . At this position, the receiver is only positively coupled with the third transmitter, so the current I_3 is high and the other currents are close to zero.

The peak voltage and current stresses of the circuit components are also acquired from circuit simulation, which is shown in **Table V**. The MOSFETs can achieve soft switching, so the peak voltage stress is the input dc voltage 180 V and the peak current stress is 22 A. For the diodes, the peak voltage stress is the output dc voltage 150 V, and the peak current stress is also 22 A. For the compensation capacitors, the capacitor C_a has the highest voltage stress and the capacitor C_{fa} has the highest current stress. Therefore, in the prototype, multiple capacitors should be connected in series and parallel to acquire higher voltage and current ratings.

The magnetic field around the system is also simulated. The receiver position $p_o = 776$ mm is again set as the example point, which is shown in **Fig. 9**. Since aluminum shielding is used with the transmitters and receiver, the emission of magnetic fields is reduced. The International Commission on Non-Ionizing Radiation Protection (ICNIRP) has published the latest guidelines for safe operation in 2010, which is called ICNIRP 2010 [32]. They require that the exposure limitation of magnetic field for the general public is 27 μ T at 85 kHz. **Fig. 9** shows that the emission of magnetic fields is below the safety requirement at a distance of 400 mm away from the system.



Fig. 10. Structure and dimension of primary transmitter coils P_1 , P_2 , and P_3 .

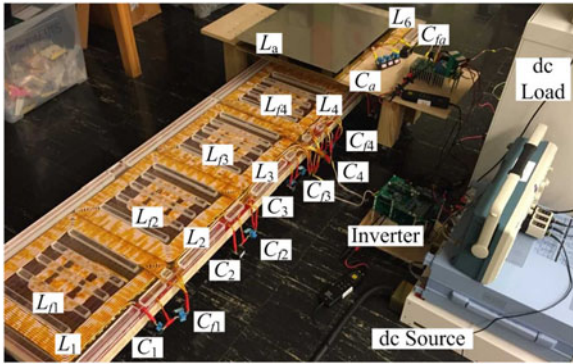


Fig. 11. Experimental prototype of the dynamic charging system.

V. EXPERIMENTS

A prototype is constructed with all the coil parameters in Section II and the compensation parameters in Section IV. The structure and dimension of the primary transmitters coils $P_1 - P_3$ are shown in Fig. 10. The aluminum sheet is the bottom layer, the ferrite plate is placed in the middle, and the transmitter coils and compensation inductors the top layer. The ferrite plate dimensions are larger than the coils to increase the coupling, and the aluminum sheet dimensions are larger than the ferrite to provide better shielding.

The compensation inductors L_{fi} ($i = 1, 2, \dots, 6$) are integrated inside the transmitter coils [33]. This can help to reduce the system size. The transmitters have a unipolar structure and the compensation inductors have a bipolar structure, which helps to eliminate the coupling between the transmitters and the inductors. Using these transmitters, the dynamic system prototype is shown in Fig. 11.

All six transmitter coils are identical and connected in parallel. They share a single full-bridge inverter. The rectifier and its compensation circuit are connected to a dc load through a rectifier, which operates in constant voltage mode. The compensation inductors are integrated into the main coils to save space. The main coils are made from 1900-strand AWG 38 Litz-wire, and the inductors L_{fi} and L_{fa} use 800-strand AWG 38 Litz-wire. The ferrite plate material is PE40 from TDK. A general-purpose full-bridge inverter is used at the primary side to provide ac excitation. It contains four silicon carbide (SiC) MOSFETs (C2M0025120D) with a rating voltage of 1.2 kV. In future

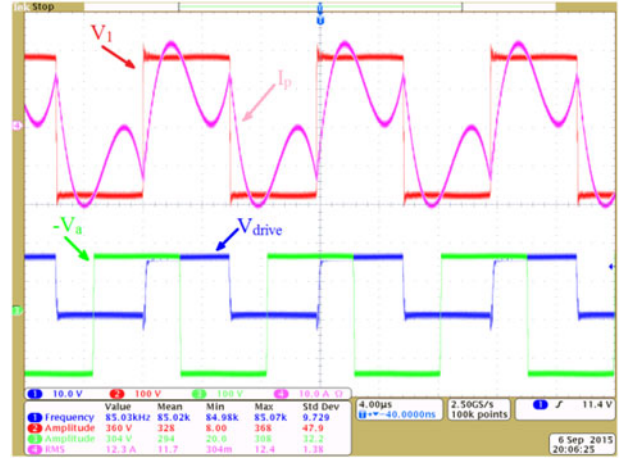


Fig. 12. Experimental waveforms of the dynamic charging system. Horizontal time period: $4.0 \mu\text{s}/\text{div}$. Channel 1 (blue): driver voltage V_{drive} , $10 \text{ V}/\text{div}$. Channel 2 (red): input voltage V_1 , $100 \text{ V}/\text{div}$. Channel 3 (green): output voltage $-V_a$, $100 \text{ V}/\text{div}$. Channel 4 (pink): input current I_p , $10 \text{ A}/\text{div}$.

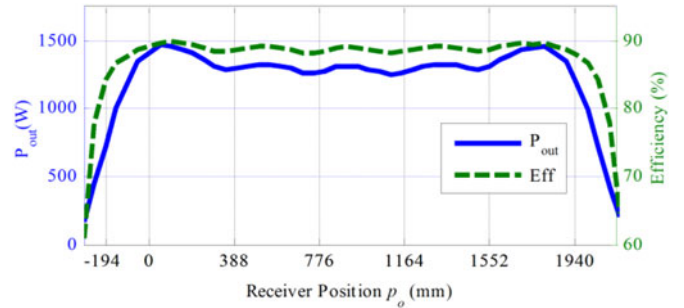


Fig. 13. System output power and efficiency along the transmitter track.

research, the power level of the prototype will be increased and this inverter will continue to be used in the high power system. The output rectifier adopts SiC diodes (IDW30G65C5) with a voltage rating of 650 V, which can also be used in the future high power system.

When the receiver position $p_o = 776 \text{ mm}$, the experimental voltage and current waveforms are shown in Fig. 12, which are similar to the simulated waveforms in Fig. 8. The output voltage V_a is inverted by 180° due to the connection of the voltage probe. The inverter achieves a soft-switching condition.

When the receiver moves along the transmitters, the output power and efficiency are shown in Fig. 13. The shape of the output power waveform is similar to the coupling coefficient in Fig. 4. The output power stays about 1.4 kW with a variation of $\pm 7.5\%$, over the entire range. When considering the middle section (388 mm, 1445 mm), the output power variation is only $\pm 2.9\%$. From the dc source to the dc load, the system's highest efficiency is 89.78%.

Using the circuit components model presented in [34], the power loss in each component can be estimated, as shown in Fig. 14. The ferrite consumes the highest power of all the components, so the system efficiency can be improved through using better magnetic materials and optimizing the design of the ferrite.

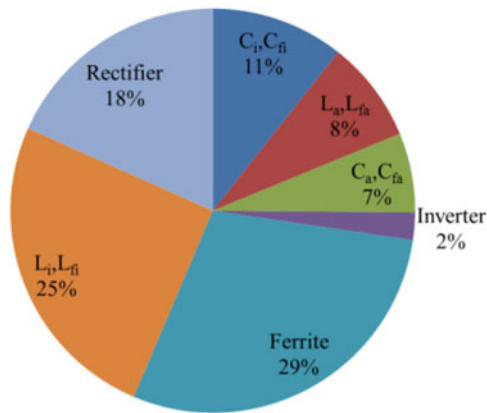


Fig. 14. Power loss distribution in the circuit components.

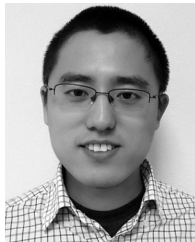
VI. CONCLUSION

This paper has proposed a dynamic charging system that reduces the power pulsations in a dynamic charging system. The transmitters are placed next to each other to eliminate power dips between coils. The receiver size is optimized to maintain a relatively constant coupling coefficient with the transmitters. The double-sided LCC-compensation network is adopted in this paper, considering the coupling between the transmitter coils. A 1.4-kW prototype was constructed to validate the design. The experimental results show a $\pm 7.5\%$ power ripple in the whole range, and $\pm 2.9\%$ ripple in the middle section. The system efficiency from dc source to dc load reaches 89.78%.

REFERENCES

- [1] G. A. Covic and J. T. Boys, "Modern trends in inductive power transfer for transportation applications," *IEEE J. Emerg. Sel. Topics Power Electron.*, vol. 1, no. 1, pp. 28–41, Mar. 2013.
- [2] S. Lukic and Z. Pantic, "Cutting the cord: Static and dynamic inductive wireless charging of electric vehicle," *IEEE Electrific. Mag.*, vol. 1, no. 1, pp. 57–64, Sep. 2013.
- [3] J. Deng, F. Lu, S. Li, T. Nguyen, and C. Mi, "Development of a high efficiency primary side controlled 7kW wireless power charger," in *Proc. IEEE Int. Elect. Veh. Conf.*, 2014, pp. 1–6.
- [4] J. Deng, F. Lu, W. Li, R. Ma, and C. Mi, "ZVS double-sided LCC compensated resonant inverter with magnetic integration for electric vehicle wireless charger," in *Proc. IEEE Appl. Power Electron. Conf.*, 2015, pp. 1131–1136.
- [5] S. Y. Choi, B. W. Gu, S. Y. Jeong, and C. T. Rim, "Advances in wireless power transfer systems for roadway-powered electric vehicles," *IEEE J. Emerg. Sel. Topics Power Electron.*, vol. 3, no. 1, pp. 18–36, Mar. 2015.
- [6] S. Jeong, Y. J. Jang, and D. Kum, "Economic analysis of the dynamic charging electric vehicle," *IEEE Trans. Power Electron.*, vol. 30, no. 11, pp. 6368–6377, Nov. 2015.
- [7] J. Li, P. T. Jones, O. Onar, and M. Starke, "Coupling electric vehicles and power grid through charging-in-motion and connected vehicle technology," in *Proc. IEEE Int. Elect. Veh. Conf.*, 2014, pp. 1–7.
- [8] A. Gilchrist, H. Wu, and K. Sealy, "Novel system for wireless in-motion EV charging and disabled vehicle removal," in *Proc. IEEE Int. Elect. Veh. Conf.*, 2012, pp. 1–4.
- [9] S. Chopra and P. Bauer, "Driving range extension of EV with on-road contactless power transfer—A case study," *IEEE Trans. Ind. Electron.*, vol. 60, no. 1, pp. 329–338, Jan. 2013.
- [10] J. Shin, S. Shin, Y. Kim, S. Ahn, S. Lee, G. Jung, S. Jeon, and D. Cho, "Design and implementation of shaped magnetic-resonance-based wireless power transfer system for roadway-powered moving electric vehicle," *IEEE Trans. Ind. Electron.*, vol. 61, no. 3, pp. 1179–1192, Mar. 2014.
- [11] V. Prasanth and P. Bauer, "Distributed IPT systems for dynamic powering misalignment analysis," *IEEE Trans. Ind. Electron.*, vol. 61, no. 11, pp. 6013–6021, Nov. 2014.
- [12] F. Pijl, M. Castilla, and P. Bauer, "Adaptive slide-mode control for a multiple-user inductive power transfer system without need for communication," *IEEE Trans. Ind. Electron.*, vol. 60, no. 1, pp. 271–279, Jan. 2013.
- [13] J. M. Miller, O. C. Onar, C. P. White, and S. Campbell, "Demonstrating dynamic wireless charging of an electric vehicle: The benefit of electrochemical capacitor smoothing," *IEEE Power Electron. Mag.*, vol. 1, no. 1, pp. 12–24, Mar. 2014.
- [14] G. A. Covic, J. T. Boys, M. Kissin, and H. G. Lu, "A three-phase inductive power transfer system for roadway-powered vehicles," *IEEE Trans. Ind. Electron.*, vol. 54, no. 6, pp. 3370–3378, Dec. 2007.
- [15] M. Kissin, J. T. Boys, and G. A. Covic, "Interphase mutual inductance in polyphase inductive power transfer systems," *IEEE Trans. Ind. Electron.*, vol. 56, no. 7, pp. 2393–2400, Jul. 2009.
- [16] W. Y. Lee, J. Huh, S. Y. Choi, X. Thai, J. Kim, E. Al-Ammar, A. El-Kady, and C. T. Rim, "Finite-width magnetic mirror models of mono and dual coils for wireless electric vehicles," *IEEE Trans. Power Electron.*, vol. 28, no. 3, pp. 1413–1428, Mar. 2013.
- [17] Y. D. Ko and Y. J. Jang, "The optimal system design of the online electric vehicle utilizing wireless power transmission technology," *IEEE Trans. Intell. Transp. Syst.*, vol. 14, no. 3, pp. 1255–1265, Sep. 2013.
- [18] Y. J. Jang, E. S. Suh, and J. W. Kim, "System architecture and mathematical models of electric transit bus system utilizing wireless power transfer technology," *IEEE Syst. J.*, to be published, doi: 10.1109/JSYST.2014.2369485.
- [19] S. Choi, J. Huh, W. Y. Lee, S. W. Lee, and C. T. Rim, "New cross-segmented power supply rails for roadway-powered electric vehicle," *IEEE Trans. Power Electron.*, vol. 28, no. 12, pp. 5832–5841, Dec. 2013.
- [20] S. Choi, B. Gu, S. W. Lee, W. Y. Lee, J. Huh, and C. T. Rim, "Generalized active EMF cancel methods for wireless electric vehicles," *IEEE Trans. Power Electron.*, vol. 29, no. 11, pp. 5770–5783, Nov. 2014.
- [21] J. Huh, S. W. Lee, W. Y. Lee, G. H. Cho, and C. T. Rim, "Narrow-width inductive power transfer system for online electric vehicle," *IEEE Trans. Power Electron.*, vol. 26, no. 12, pp. 3666–3679, Dec. 2011.
- [22] S. Y. Choi, J. Huh, W. Y. Lee, and C. T. Rim, "Asymmetric coil set for wireless stationary EV chargers with lateral tolerance by dominant field analysis," *IEEE Trans. Power Electron.*, vol. 29, no. 12, pp. 6406–6420, Dec. 2014.
- [23] G. A. Elliott, S. Raabe, G. A. Covic, and J. T. Boys, "Multiphase pick-ups for large lateral tolerance contactless power-transfer systems," *IEEE Trans. Ind. Electron.*, vol. 57, no. 5, pp. 1590–1598, May 2010.
- [24] S. Raabe and G. A. Covic, "Practical design considerations for contactless power transfer quadrature pick-ups," *IEEE Trans. Ind. Electron.*, vol. 60, no. 1, pp. 400–409, Jan. 2013.
- [25] S. Li, W. Li, J. Deng, T. D. Nguyen, and C. C. Mi, "A double-sided LCC compensation network and its tuning method for wireless power transfer," *IEEE Trans. Veh. Technol.*, vol. 64, no. 6, pp. 2261–2273, Jun. 2015.
- [26] S. Li and C. C. Mi, "Wireless power transfer for electric vehicle applications," *IEEE J. Emerg. Sel. Topics Power Electron.*, vol. 3, no. 1, pp. 4–17, Mar. 2015.
- [27] O. C. Onar, J. M. Miller, S. Campbell, C. Coomer, C. White, and L. Seiber, "A novel wireless power transfer for in-motion EV/PHEV charging," in *Proc. IEEE Appl. Power Electron. Conf.*, 2013, pp. 3073–3080.
- [28] J. M. Miller, P. T. Jones, J. Li, and O. C. Onar, "ORNL experience and challenges facing dynamic wireless power charging of EV's," *IEEE Circuits Syst. Mag.*, vol. 15, no. 2, pp. 40–53, May 2015.
- [29] K. Lee, Z. Pantic, and S. M. Lukic, "Reflexive field containment in dynamic inductive power transfer systems," *IEEE Trans. Power Electron.*, vol. 29, no. 9, pp. 4592–4602, Sep. 2014.
- [30] L. Chen, G. R. Nagendra, J. T. Boys, and G. A. Covic, "Double-coupled systems for IPT roadway applications," *IEEE J. Emerg. Sel. Topics Power Electron.*, vol. 3, no. 1, pp. 37–49, Mar. 2015.
- [31] Z. Popovic and B. D. Popovic, *Introductory Electromagnetics, Practice Problems and Labs*. Englewood Cliffs, NJ, USA: Prentice-Hall, 2000.
- [32] International Commission on Non-Ionizing Radiation Protection, "IC-NIRP guidelines for limiting exposure to time-varying electric, magnetic and electromagnetic fields (1 Hz to 100 kHz)," *Health Phys.*, vol. 99, pp. 818–836, 2010.
- [33] J. Deng, F. Lu, R. Ma, and C. C. Mi, "ZVS double-side LCC compensated resonant inverter with magnetic integration for electric vehicle wireless charger," in *Proc. IEEE Appl. Power Electron. Conf.*, 2015, pp. 1131–1136.

- [34] F. Lu, H. Hofmann, J. Deng, and C. C. Mi, "Output power and efficiency sensitivity to circuit parameter variations in double-sided LCC-compensated wireless power transfer system," in *Proc. IEEE Appl. Power Electron. Conf.*, 2015, pp. 507–601.



Fei Lu (S'12) received the B.S. and M.S. degrees in electrical engineering from Harbin Institute of Technology, Harbin, China, in 2010 and 2012, respectively. He is currently working toward the Ph.D. degree in electrical engineering at the University of Michigan, Ann Arbor, MI, USA.

His research focuses on wireless power transfer for the application of electric vehicle charging. He is working on high-power and high-efficiency capacitive power transfer through an air-gap distance up to 100s of millimeters. He is also working on dynamic charging of electric vehicles, which allows the vehicle to be continuously charged while moving.



Hua Zhang (S'14) received the B.S. and M.S. degrees in electrical engineering from Northwestern Polytechnical University, Xi'an, China, in 2011 and 2014, respectively, where she is currently working toward the Ph.D. degree in electrical engineering. From September 2014 to August 2015, she was a joint Ph.D. student funded by the China Scholarship Council with the University of Michigan, Dearborn, MI, USA.

In September 2015, she joined San Diego State University, San Diego, CA, USA. Her research concerns the coupler design of high-power inductive power transfer and capacitive power transfer systems.



Heath Hofmann (M'89–SM'15) received the B.S. degree in electrical engineering from The University of Texas at Austin, Austin, TX, USA, in 1992, and the M.S. and Ph.D. degrees in electrical engineering and computer science from the University of California, Berkeley, CA, USA, in 1997 and 1998, respectively.

He is currently an Associate Professor with the University of Michigan, Ann Arbor, MI, USA. His research interests include the design, analysis, and control of electromechanical systems, and power electronics.



Chunting Chris Mi (S'00–A'01–M'01–SM'03–F'12) received the B.S.E.E. and M.S.E.E. degrees from Northwestern Polytechnical University, Xi'an, China, in 1985 and 1988, respectively, and the Ph.D. degree from the University of Toronto, Toronto, ON, Canada, in 2001, all electrical engineering.

He is a Professor and Chair of Electrical and Computer Engineering and the Director of the Department of Energy-funded Graduate Automotive Technology Education Center for Electric Drive Transportation, San Diego State University (SDSU), San Diego, CA, USA. Prior to joining SDSU, he was with University of Michigan, Dearborn, MI, USA, from 2001 to 2015. His research interests include electric drives, power electronics, electric machines, renewable-energy systems, and electrical and hybrid vehicles. He has conducted extensive research and has published more than 100 journal papers.